Neurosci. Bull. January, 2020, 36(1):49–65
https://doi.org/10.1007/s12264-019-00415-3

www.neurosci.cn
www.springer.com/12264

ORIGINAL ARTICLE

# Distribution and Functional Characteristics of Voltage-Gated Sodium Channels in Immature Cochlear Hair Cells

**You Zhou[1,2,3] · Chenchen Xia[4] · Manli Yin[4] · Xueling Wang[1,2,3] · Hao Wu[1,2,3] · Yonghua Ji[4,5]**

Received: 10 March 2019 / Accepted: 15 April 2019 / Published online: 6 August 2019


**Abstract** Voltage-gated sodium channels (VGSCs) are transiently expressed in cochlear hair cells before hearing onset and play an indispensable role in shaping spontaneous activity. In this study, we showed that $Na^+$ currents shaped the spontaneous action potentials in developing mouse inner hair cells (IHCs) by decreasing the time required for the membrane potential to reach the action-potential threshold. In immature IHCs, we identified 9 known VGSC subtypes (Nav1.1α–1.9α), among which Nav1.7α was the most highly expressed subtype and the main contributor to $Na^+$ currents in developing hair cells. Electrophysiological recordings of two cochlea-specific Nav1.7 variants (CbmNav1.7a and CbmNav1.7b) revealed a novel loss-of-function mutation (C934R) at the extracellular linker between segments 5 and 6 of domain II. In addition, post-transcriptional modification events, such as alternative splicing and RNA editing, amended the gating properties and kinetic features of $CbmNav1.7a_{(C934)}$. These results provide molecular and functional characteristics of VGSCs in mammalian IHCs and their contributions to spontaneous physiological activity during cochlear maturation.

**Keywords** Cochlear hair cell · Spontaneous action potential · Voltage-gated sodium channel · Post-transcriptional modification · Gating property

## Introduction

Hair cells, the primary sensory receptors of the mammalian cochlea, relay sound information to the brain *via* the coordinated release of neurotransmitters to activate spiral ganglion neurons [1]. Before the onset of hearing [at about postnatal days (P) 12–13 in most altricial rodents], inner hair cells (IHCs) cannot respond to sound but instead generate spontaneous action potentials that are sufficient to induce the release of vesicles [2]. The spontaneous activity originating from IHCs is involved in regulating a variety of cellular responses and the refinement of downstream neuronal circuits in developing auditory systems [3, 4]. Although spontaneous action potentials in premature IHCs are mainly due to interplay between an inward $Ca^{2+}$ current and a delayed rectifier $K^+$ current, they are also modulated by other transiently-expressed conductance events, such as the small-conductance $Ca^{2+}$-sensitive $K^+$ (SK2) current [5]. The SK2 channel is not required to generate spontaneous action potentials but is essential for sustaining continuous repetitive spontaneous activity in pre-hearing IHCs and for the functional maturation of IHCs

**Electronic supplementary material** The online version of this article (https://doi.org/10.1007/s12264-019-00415-3) contains supplementary material, which is available to authorized users.

✉ Hao Wu
wuhao622@sina.cn

✉ Yonghua Ji
yhji@staff.shu.edu.cn

1 Department of Otolaryngology – Head and Neck Surgery, Ninth People's Hospital, Shanghai Jiaotong University School of Medicine, Shanghai 200125, China

2 Ear Institute, Shanghai Jiaotong University School of Medicine, Shanghai 200125, China

3 Shanghai Key Laboratory of Translational Medicine on Ear and Nose Diseases, Shanghai 200125, China

4 Laboratory of Neuropharmacology and Neurotoxicology, Shanghai University, Shanghai 200444, China

5 Translational Institute for Cancer Pain, Xinhua Hospital Chongming Branch, Shanghai 202150, China

[6]. The $Na^+$ current is also transiently expressed in developing IHCs and is speculated to be involved in shaping spontaneous cochlear activity before the onset of hearing [7, 8]. In contrast, outer hair cells (OHCs) at the pre-hearing stage do not show spontaneous action potentials, but rather exhibit a single $Ca^{2+}$-dependent action potential following depolarizing injections of current [9]. Similar to IHCs, immature OHCs produce a repertoire of membrane currents including $Na^+$ currents [10]. The role of $Na^+$ currents in immature OHCs has not been reported to date, and it is worthwhile to investigate the functional maturation and acquisition of electromotile activity before the onset of hearing [11].

It is well known that voltage-gated $Na^+$ channels (VGSCs) are essential for the generation and propagation of action potentials in most excitable tissues. VGSCs are membrane protein complexes generally composed of one primary α subunit and two auxiliary β subunits [12]. To date, 9 subunit isoforms ($Na_V1.1\alpha$–$1.9\alpha$) have been discovered in mammalian cells; Nav1.1α, 1.2α, 1.3α, and 1.6α are predominantly expressed in the central nervous system; Nav1.7α, 1.8α, and 1.9α are preferentially distributed in peripheral sensory neurons; and Nav1.4α and 1.5α are selectively expressed in skeletal muscle cells and cardiac cells, respectively [13]. The 9 VGSC subtypes are highly homologous in terms of sequence and structure; however, their gating characteristics, pharmacological properties, tissue distribution, and physiological functions are subtly diverse and specific [14]. In developing vestibular hair cells, two types of $Na^+$ current have been identified, namely a tetrodotoxin (TTX)-sensitive current that might be carried by Nav1.2α and 1.6α, and a TTX-insensitive current carried by Nav1.5α [15, 16]. However, the $Na^+$ current in developing IHCs has been shown to be highly sensitive to TTX [8, 17]. Our previous study revealed that all known subtypes of VGSCs are expressed in mouse cochlear sensory epithelia before the onset of hearing and that various VGSC splicing variants might be important to adapt to the unique physiological properties of the immature cochlea [18]. These results point to pivotal roles for VGSCs in regulating spontaneous activity in the developing cochlea.

To understand the physiological roles of VGSCs in pre-hearing hair cells, we aimed to investigate the following: (1) how the $Na^+$ current is involved in regulating spontaneous activity; (2) which subtype mainly contributes to the $Na^+$ current; and (3) whether cochlea-specific VGSC variants exhibit distinct gating properties.

## Materials and Methods

### Experimental Animals

C57BL6 mice [pregnant and newborn (P3–P7)] were obtained from the Shanghai Laboratory Animal Center (Chinese Academy of Sciences, Shanghai, China) and maintained under a 12/12 h light/dark cycle, with standard food and water provided *ad libitum*. The infant mice used in this work were killed by acute decapitation using dissecting scissors, and then quickly transferred into pre-cooled solution for dissection of the cochlea. The experimental procedures described here were performed in accordance with the National Institutes of Health (NIH) guidelines for the Care and Use of Laboratory Animals and were approved by the Ethics Committee and the Committee of Animal Experimentation at Shanghai University. All efforts were made to minimize the number of animals used and their suffering.

### Tissue Preparation

The cochleas used for electrophysiological recording were dissected in extracellular solution composed of (in mmol/L): 135 NaCl, 5.8 KCl, 1.3 $CaCl_2$, 0.9 $MgCl_2$, 0.7 $NaH_2PO_4$, 5.6 D-glucose, 10 Hepes-NaOH, 2 sodium pyruvate, 50× MEM amino acid solution (Invitrogen, Carlsbad, CA) and 100× MEM vitamin solution (Invitrogen) (pH 7.5, 308 mOsmol/kg). The extracellular solution was saturated with $O_2$ and cooled before cochlea dissection. The cochleas collected for RNA extraction and immunohistochemistry were dissected in ice-cold artificial cerebral spinal fluid (ACSF) containing the following (in mmol/L): 124 NaCl, 2.5 KCl, 1.3 $CaCl_2$, 1.3 $MgCl_2$, 1.25 $NaH_2PO_4$, 26 $NaHCO_3$, and 11 D-glucose (pH 7.4, 295 mmol/kg). The ACSF was saturated with 95% $O_2$ and 5% $CO_2$. Intact sensory epithelia were acquired by carefully removing the stria vascularis, vestibular membrane, spiral ganglion, and tectorial membrane using fine forceps.

### Whole-Cell Electrophysiological Recordings from Hair Cells

The dissected cochleas ($n$ = 15 mice) were transferred into a microscope chamber and immobilized under a nylon mesh attached to a platinum steel ring. Extracellular solution was continuously perfused at ∼30 mL/h using a peristaltic pump (BT100-2J, Longer, Baoding, Hebei, China). The extracellular solution and chamber were maintained close to body temperature (35 °C–37 °C) using a dual-channel heater controller (TC-344B, Warner Instruments, Hamden, CT). The organ of Corti was viewed under

an upright infrared microscope (IX71, Olympus, Tokyo, Japan). Voltage- and current-clamp recordings were performed based on the whole-cell patch-clamp technique using an Axon 700B amplifier (Molecular Devices, Sunnyvale, CA). Patch pipettes were pulled from soda glass capillaries (Weitan Technology, Changsha, Hunan, China) using a horizontal microelectrode puller (P-1000, Sutter Instrument, Novato, CA) and the electrode resistances in extracellular solution were 3 MΩ–5 MΩ. For $Na^+$ current recordings under voltage-clamp conditions, the pipette solution contained (in mmol/L): 131 CsCl, 3 $MgCl_2$, 1 EGTA-CsOH, 5 $Na_2ATP$, 5 Hepes-KOH, and 10 sodium phosphocreatine (pH 7.3, 292 mOsmol/kg). The $Ca^{2+}$-free extracellular solution for $Na^+$ current recordings contained (in mmol/L): 135 NaCl, 5.8 KCl, 3.9 $MgCl_2$, 0.7 $NaH_2PO_4$, 5.6 D-glucose, 10 Hepes-NaOH, 2 sodium pyruvate, 50× MEM amino acids (Invitrogen), and 100× MEM Vitamin solution (Invitrogen) (pH 7.5, 308 mOsmol/kg). For action potential recordings under current-clamp conditions, the pipette solution contained (in mmol/L): 131 KCl, 3 $MgCl_2$, 1 EGTA-KOH, 5 $Na_2ATP$, 5 Hepes-KOH, and 10 sodium phosphocreatine (pH 7.3, 292 mOsmol/kg). The extracellular solution for action potential recordings was the same as that used for dissection of cochleas. To investigate the function of $Na^+$ current, 500 nmol/L TTX was added to the extracellular solution to block $Na^+$ channels. To investigate the function of $Ca^{2+}$ current, we used $Ca^{2+}$-free extracellular solution in which $MgCl_2$ was increased to 3.9 mmol/L to maintain approximately constant membrane charge [8, 19]. The two extracellular solutions (with 1.3 mmol/L $Ca^{2+}$ and $Ca^{2+}$-free) for voltage- and current-clamp recordings were both saturated with $O_2$. Data were acquired using pClamp software with a DigiData 1440A data-acquisition board (Axon Instruments, Burlingame, CA). Voltage recordings were sampled at 5 and 50 kHz and low-pass filtered at 2.5 and 10 kHz (eight-pole Bessel). For current recordings, data were sampled at 100 kHz and low-pass filtered at 10 kHz using an eight-pole Bessel, the series resistance errors were compensated by 80%, and the leak conductance was subtracted using the P/N protocol. Data were analyzed off-line using Origin software (Origin Lab, Northampton, MA).

## Quantitative RT-PCR (qPCR)

The intact cochlear sensory epithelia from 25 mice (P3–P7) were collected and total RNA was extracted using TRIzol reagent (Invitrogen) according to the manufacturer's protocol. RNA integrity was confirmed with the Agilent 2100 Bioanalyzer (Agilent Technologies, Santa Clara, CA), showing clear characteristic peaks at 28S and 18S. First-strand cDNA was synthesized from total RNA using oligo (dT)18 and PrimeScript RTase (Cat#: RR037Q, Takara, Dalian, China). The short mRNA fragments encoding the 9 VGSC subtypes and $Ca_v1.3$ were then cloned by RT-PCR and the cloned fragments were sequenced to ensure the specificity of the primers (listed in Table S1). For single-cell qPCR, the intact cochlear sensory epithelia from seven P6 mice were placed in a microscope chamber and immobilized under a nylon mesh attached to a platinum-steel ring. After incubation (35 °C–37 °C) in extracellular solution with 0.625 mg/mL trypsin for 5 min, samples were washed by perfusion and cleaned using a stream of fluid from a pipette; then single IHC and OHC from the apical or basal sensory epithelium were each aspirated into a pipette filled with RNase-free extracellular solution (Recombinant RNase Inhibitor; Cat#: 2313A, Takara), and then transferred to a pre-cooled PCR tube. The synthesis of first-strand cDNA and qPCR were performed according to the manufacturer's protocol (SYBR qPCR Mix; QPS-201, Toyobo, Osaka, Japan).

## Tissue Immunohistochemistry

The apical-middle coil of sensory epithelia from 40 P6 mice were dissected and fixed in 4% paraformaldehyde for 2 h at 4 °C. The cochleas were then washed three times with 0.1 mol/L phosphate buffer solution (PBS, pH 7.4) for 5 min each and incubated in 0.5% Triton X-100 containing 3% $H_2O_2$ for 30 min at room temperature. After washing with PBS, samples were antigen-repaired for 25 min with pepsin at 37 °C. The cochleas were then washed three times and blocked for 1 h with 5% goat albumin serum at room temperature. Primary antibodies against myosin 7α (Abcam, Cambridge, UK; 1:100), Nav1.1α (Abcam; 1:500), Nav1.2α (Abcam; 1:500), Nav1.3α (Santa Cruz, San Francisco, CA; 1:50), Nav1.4α (Abcam; 1:500), Nav1.5α (Abcam; 1:500), Nav1.6α (Alomone, Jerusalem, Israel; 1:300), Nav1.7α (Abcam; 1:300), Nav1.8α (Abcam; 1:500), and Nav1.9α (Abcam; 1:200) were diluted in 5% goat serum. After incubation at 4 °C for 24 h, the samples were washed three times in PBS and then incubated with the Cys- and FITC-conjugated secondary antibodies (Abcam; 1:500) at room temperature for 1 h. The sensory epithelia were dehydrated, cover-slipped, and photographed under an upright fluorescence microscope (Nikon, Sendai, Japan).

## Transcriptome Analysis

The cochlear sensory epithelium was acutely dissected from 90 C57BL6 mice at P5–P7 and each detached into apical and basal sensory epithelia using a microelectrode. Three cDNA libraries of independent apical samples (Apex-1, Apex-2, and Apex-3) and three cDNA libraries

of independent basal samples (Base-1, Base-2, and Base-3) were constructed according to Illumina's instructions (Shanghai Personalbio Co., China). The mRNA was isolated using magnetic oligo (dT) beads. Fragmentation buffer was added to cleave the mRNA into short fragments, and these fragments were used as templates. Random hexamer-primers were used to synthesize first-strand cDNA. Buffer, dNTPs, RNase H, and DNA polymerase I were used to synthesize second-strand cDNA. Then, the fragments were purified using a QiaQuick PCR extraction kit (Qiagen, Hilden, Germany) and resolved with elution buffer for end repair and poly (A) addition. The resulting short fragments were then connected to sequencing adapters. Fragments with a suitable range of lengths were selected based on the results of agarose gel electrophoresis and were used as templates for library amplification. Library quantification was performed using Pico green and a fluorescence spectrophotometer (Quantifluor-ST fluorimeter, Promega; Quant-iT Pico Green dsDNA Assay Kit, Invitrogen). The library quality was confirmed using the Agilent 2100 Bioanalyzer and Agilent High Sensitivity DNA Kit (Agilent Technologies). Finally, the library was pair-end sequenced using Illumina NestSeq 500. Raw image data generated by sequencing were stored in fastq format and submitted to the National Center for Biotechnology Information Sequence Read Archive database (accession number: PRJNA505942).

Raw sequencing data were filtered to remove low-quality reads before subsequent analyses. Quality analysis by means of FastQC showed that the average quality of the filtered data was very high. Theoretical values coincided well with the measured values (Table S2). To annotate all useful reads, the clean reads were mapped to the mouse genome database; RPKM (reads per kilobase per million reads) values were used to measure the expression of each gene. The DESeq package was adopted to estimate variance-mean dependence in the count data from the Illumina sequencing assays and to test for differential expression based on a model using the negative binomial distribution in accordance with equation (1): (1) $\nu = s\mu + \alpha s2\mu 2$, where $\mu$ is the expected normalized count value (estimated by the average normalized count value), s is the size factor for the sample under consideration, and $\alpha$ is the dispersion value for the unigene. Differentially-expressed genes were detected in the apical and basal samples based on average expression levels that differed at least 1.5-fold and $P$ value $< 0.05$ when comparing apical and basal samples.

## Plasmid Construction and Expression

cDNA encoding two $\alpha$ subunits of Nav1.7 variants (CbmNav1.7a and CbmNav1.7b) (GenBank Numbers: KM373695.1 and KM373696.1) cloned from the developing cochlear sensory epithelia in our previous work [18] and wild-type Nav1.7$\alpha$ from peripheral dorsal root ganglion (DRG) neurons (GenBank Number: NM-001290674.1) were synthesized and each cloned into the pIRES2 expression vector with an EGFP tag. To investigate the effects of different substitution/deletions of amino acid residues on channel properties which were induced by various posttranscriptional modification events, nine mutants (1–9) were generated and functionally compared. These related mutant plasmids were produced using sequential PCR (GenScript Biotech Corp., Nanjing, China). Mutant 1 was generated by replacing two codons in exon 5 (substituting 201V206D for 201L206N) of wtNav1.7; mutant 2 by deleting eleven codons in exon 11 (deletion of 11 amino acid residues) of mutant 1; mutant 3 by deleting exon 20 (deletion of 41 amino acid residues) of mutant 2; mutant 2 was used as the starting material to generate the 934R, 1037T, and 1643S variants (mutants 4–6); and CbmNav1.7a was used to generate the 934C, 1037I, and 1643F variants (mutants 7–9) (Table 1). HEK293T cells were used in all experiments (Shanghai Cell Bank of the Chinese Academy of Sciences, Shanghai, China). The cells were cultured in Dulbecco's modified Eagle's medium (Life Technologies, Grand Island, NY) supplemented with 10% heat-inactivated fetal bovine serum (Gibco, Grand Island, NY). Culture dishes were incubated at 37 °C in a humidified atmosphere containing 5% $CO_2$ and cultured for 2–3 days. One day before transfection, HEK293T cells were transferred into 24-well plates. At 90% confluence, the cells were transiently transfected using Lipofectamine 3000 (Invitrogen) at a ratio of 1 μL reagent to 1 μg total plasmid per well. Electrophysiological experiments were performed 1–2 days after transfection.

## Whole-Cell Electrophysiological Recordings from HEK293T Cells

Whole-cell voltage-clamp recordings were made using an Axon Multiclamp 700B Microelectrode Amplifier (Molecular Devices) at room temperature (21 °C–25 °C). Patch pipettes were fabricated from glass capillary tubes using the PC-10 Puller (Narishige, Tokyo, Japan) with resistances of 2 MΩ–3 MΩ. Data acquisition and stimulation protocols were controlled by a Pentium III computer (Legend, Beijing, China) equipped with pCLAMP10.3 (Molecular Devices). Capacitance transients were cancelled and cells with a seal resistance $< 1$ GΩ were omitted. Series resistance (Rs) was compensated (80%–90%) to minimize voltage errors, and cells with an uncompensated Rs $> 10$ MΩ were omitted. Leak subtraction was performed using the P/N protocol. Data were

**Table 1** Construction strategies of nine Nav1.7 mutants.

| Mutant 1 | Mutant 2 | Mutant 3 |
|---|---|---|
| wt Nav1.7 (L201V/N206D) | mutant 1 (647–657 deletion) | mutant 2 (1266–1306 deletion) |
| Mutant 4 | Mutant 5 | Mutant 6 |
| mutant 2 (C934R) | mutant 2 (I1037T) | mutant 2 (F1643S) |
| Mutant 7 | Mutant 8 | Mutant 9 |
| CbmNav1.7a (R934C) | CbmNav1.7a (T1037I) | CbmNav1.7a (S1634F) |

Note: Mutants 1–3 were employed to analyze the substitution/deletion of amino acid residues respectively induced by three alternative splicing events. Mutants 4–6 were constructed to analyze the substitution of amino acid residues induced by three RNA editing events. Mutants 7–9 were generated for backward verification of the effects of three RNA editing events on channel properties.

sampled at 50 kHz and low-pass filtered at 10 kHz. The extracellular solution contained (in mmol/L): 140 NaCl, 3 KCl, 1 $MgCl_2$, 1.5 $CaCl_2$, 10 D-glucose, and 10 Hepes-NaOH (pH 7.4, 320 mOsmol/kg). The pipette solution contained (in mmol/L): 131 CsCl, 3 $MgCl_2$, 1 EGTA-CsOH, 5 $Na_2ATP$, 5 Hepes-CsOH, and 10 sodium phosphocreatine (pH 7.3, 292 mOsmol/kg).

$Na^+$ currents were elicited by 100-ms depolarizing pulses to + 80 mV from a holding potential of − 100 mV. Mean conductance ($G$) was calculated from peak current-voltage relationships using equation (2) as follows: (2) $G = I/(V - Vr)$, where $I$ is the peak current elicited by depolarization, $V$ is the membrane potential, and $Vr$ is the reversal potential. The voltage dependence for activation was fitted using the Boltzmann relationship as follows (equation 3): (3) $G/G\max = 1/[1 + \exp(V - Vm)/k_m]$, where $Vm$ is the voltage for half-maximum activation and $k_m$ is the slope factor. Current decays were fitted using a double-exponential equation (4) as follows: (4) $I = A_{fast} \times \exp[-(t - K)/\tau_{fast}] + A_{slow} \times \exp[-(t - K)/\tau_{slow}] + I_{SS}$, where $I$ is the current, $A_{fast}$ and $A_{slow}$ represent the percentages of channels inactivating with time constants $\tau_{fast}$ and $\tau_{slow}$, $t$ is the conditioning pulse duration, $K$ is the time shift, and $I_{SS}$ is the steady-state asymptote. The voltage-dependence of the steady-state inactivation and fast inactivation data was described using the two-state Boltzmann equation (5) as follows: $I/I\max = 1/[1 + \exp(V - V_{1/2})/k]$, where $V$ is the membrane potential of the conditioning step, $V_{1/2}$ is the membrane potential at which half-maximal inactivation is achieved, and $k$ is the slope factor. Recovery data were fitted with a single-exponential equation (6) as follows: (6) $I/I_{peak} = 1 - A \times \exp(-t/\tau_{rec})$, where $A$ is the relative proportion of current recovering with time constant $\tau_{rec}$, and $t$ is the recovery interval. Voltage-dependent deactivation kinetics was assessed by eliciting tail currents at a range of potentials after briefly activating the channels (0 mV, 0.5 ms). The averaged voltage-plot was compiled using time constants ($\tau_d$) obtained from tail current recordings and determined by fitting each decay component with a single-exponential equation. Ramp current generation was assayed using a slow depolarizing ramp stimulus (0.27 mV/ms, 600 ms) from − 120 mV to + 40 mV at a holding potential of − 120 mV. Inward ramp currents displayed are the result of dividing the individual traces by the peak transient $Na^+$ current recorded during the $I/V$ protocol, thus yielding the percentage of peak current for each recording.

### Statistical Analysis

Data are presented as the mean ± SEM and were analyzed using Origin 8.5 (OriginLab, Northampton, MA) and GraphPad Prism 7 (GraphPad Software, La Jolla, CA). The number of cells recorded in the electrophysiological experiments is represented by $n$. The paired or unpaired Student's two-tailed $t$-test was used for two-group comparison and one-way analysis of variance (ANOVA) followed by the *post-hoc* Bonferroni test was used for multiple comparisons. $P < 0.05$ was considered statistically significant.

## Results

### Sodium Currents Shape the Action Potentials of Immature IHCs

Current-clamp recordings demonstrated that the immature IHCs generated spontaneous and evoked action potentials, which were reversibly abolished by the absence of extracellular $Ca^{2+}$ (Fig. S1). No spontaneous action potentials were detectable in developing OHCs, but single action potentials were elicited by depolarizing current injection (Fig. S2). Voltage-clamp recordings showed that typical voltage-dependent $Na^+$ currents were elicited in both IHCs and OHCs following 200-ms conditioning steps to a range of potentials from − 100 mV to + 80 mV (Fig. 1A–E). To evaluate whether $Na^+$ currents contribute to the action potentials, IHCs were further studied before

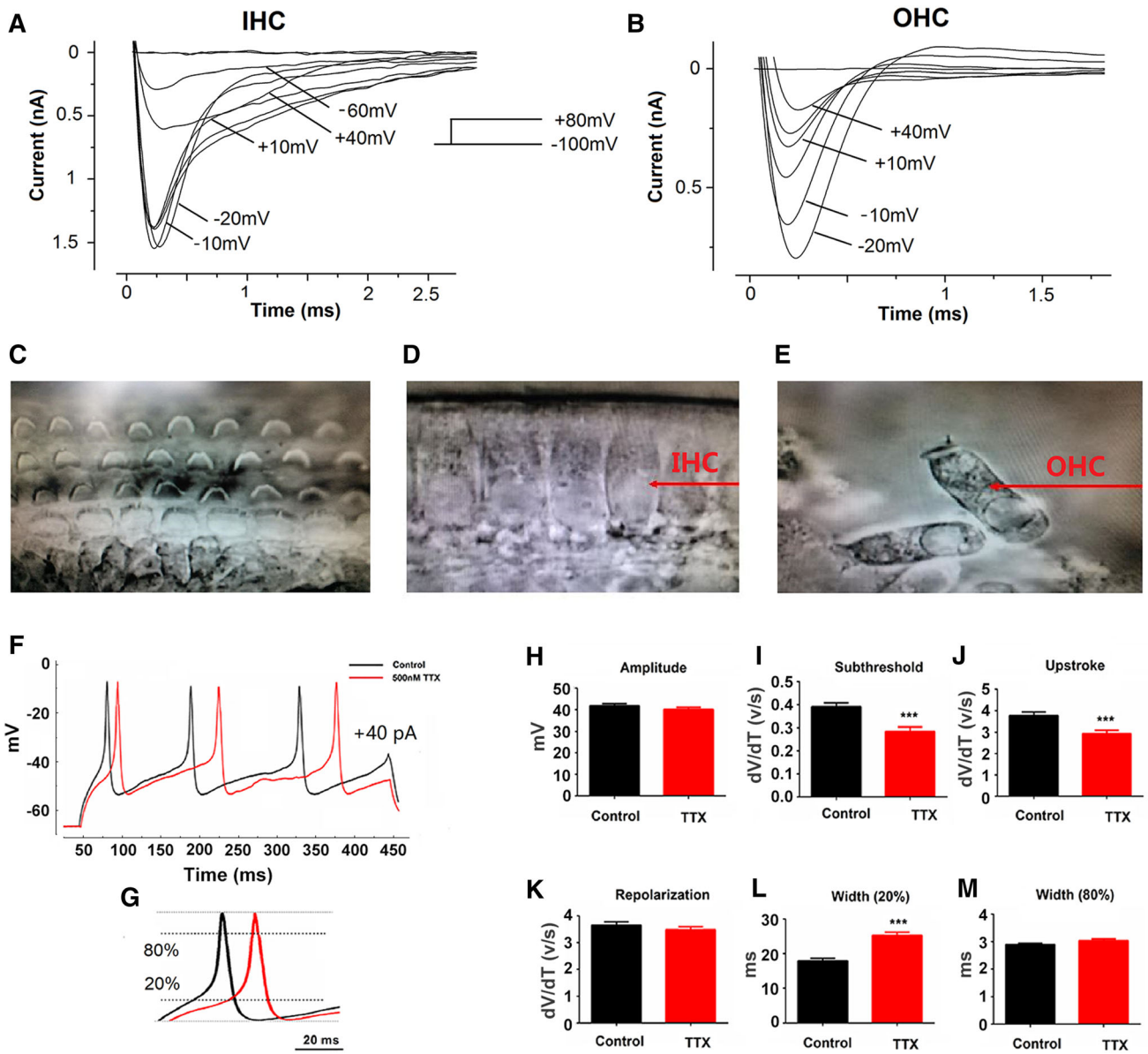


**Fig. 1** Quantitative effects of TTX on action potentials in immature hair cells. **A** $Na^+$ current recorded from a P6 IHC (apical) by applying depolarizing voltage steps from a holding potential of − 100 mV (recording conditions: $V_m$ − 60 mV, $C_m$ 7.83 pF, temperature 37 °C). **B** $Na^+$ current recorded from a P6 OHC (basal). For clarity, only some of the traces are shown and some of the potentials are shown next to them (recording conditions: $V_m$ − 62 mV, $C_m$ 8.79 pF, temperature 37 °C). **C–E** Three rows of OHCs with "V"-like stereocilia and one row of IHCs (40× water-immersion lens). **F** Action potentials evoked by +40 pA injection in a P5 IHC before (black solid line) and during superfusion (red solid line) with 500 nmol/L TTX (recording conditions: $V_m$ − 67 mV, $C_m$ 11.8 pF, temperature 37 °C). **G** Measurement of the width of the action potentials at the 20% and 80% labels (black dotted lines) between peak and maximum repolarization levels (dotted lines). **H** Amplitude of single action potentials before and during the TTX application ($n$ = 10). **I–K** Rate of subthreshold depolarization (I), upstroke (J), and repolarization (K) of single action potentials before and during TTX application ($n$ =10). **L, M** Width of action potentials measured at the two levels shown in **G** ($n$ = 10). ***$P < 0.001$, control *versus* TTX-superfusion group, paired Student's $t$-test. Data are presented as the mean ± SEM.

and after extracellular application of TTX. The extracellular application of 500 nmol/L TTX did not prevent the induced action potentials in immature IHCs, but affected their time course (Fig. 1F, G). In the presence of TTX, the amplitude (Fig. 1H) and repolarization rate (d$V$/d$t$) of action potentials were unchanged (Fig. 1K), but the subthreshold depolarization rate was significantly slower ($P < 0.001$, $n$ = 10) (Fig. 1I). The lack of $Na^+$ currents was also found to decrease the maximum rate of rise of the action potential upstroke ($P < 0.001$, $n$ = 10) (Fig. 1J). In addition, we measured the width of the action potential at levels below threshold (20% of spike height) and the action

potential proper (80% of spike height). At the subthreshold level, the width of action potentials was greater in the presence of TTX ($P < 0.001$, $n = 10$) (Fig. 1L). However, the width of the actual spike did not change significantly (Fig. 1M). These results are consistent with previous studies showing that the $Na^+$ currents in premature IHCs play a role in shaping the action potentials mainly by reducing the time necessary for the membrane potential to reach threshold [8, 17].

### Expression and Distribution of VGSC Subtypes in Immature Hair Cells

Immunolabeling experiments showed that IHCs and OHCs in the organ of Corti were specifically labeled by antibodies directed against the nine VGSC subtypes (Fig. 2A–I). Further, RT-PCR experiments revealed that all subtypes (Nav1.1α–1.9α) were present in developing cochlear sensory epithelia (Fig. 2J). Single-cell qPCR revealed that six of the subtypes (Nav1.2α, 1.3α, 1.4α, 1.5α, 1.7α, and 1.9α) were found in apical and basal IHCs, while the other three (Nav1.1α, 1.6α, and 1.8α) were expressed at extremely low levels or undetectable (Fig. 2K). On the other hand, six subtypes (Nav1.2α, 1.3α, 1.5α, 1.6α, 1.7α, and 1.9α) were detected in apical and basal OHCs, while the other three (Nav1.1α, 1.4α, and 1.8α) were only found in either apical or basal OHCs (Fig. 2L). Compared to the other eight subtypes, Nav1.7α exhibited the highest expression in immature IHCs and OHCs from apical and basal sensory epithelia, suggesting that it might be the dominant subtype that contributed to the $Na^+$ currents in developing hair cells (Fig. 2K, C). Furthermore, transcriptome analyses revealed that the α subunits of the nine VGSC subtypes and four β subunits (β1–β4) occurred in the apical and basal sensory epithelia. Among them, Nav1.5α was expressed at a higher level in apical sensory epithelia, whereas Nav1.1α and β4 were expressed at higher levels in basal sensory epithelia (differential screening criteria: fold of change $\geq 1.5$, $P < 0.05$) (Fig. 2M, N).

### Functional Characterization of Nav1.7 Variants in Cochlear Sensory Epithelia

When compared to the typical wtNav1.7 variant from peripheral DRG neurons, CbmNav1.7a and CbmNav1.7b cloned from developing cochlear sensory epithelia have been characterized by distinct molecular structures produced by three alternative splicing and three RNA editing events [18] (Fig. 3A, B). In the present study, we determined that $Na^+$ currents were not elicited from CbmNav1.7a and 1.7b upon exogenous expression in HEK293T cells (Fig. 3C–E). To identify which amino-acid replacement/deletion silenced these two Nav1.7 variants, 9 related mutants were constructed and functionally expressed in HEK293T cells (the mutation strategies are listed in Table 1). We found that mutants 1 and 2 generated $Na^+$ currents, whereas mutant 3 did not, indicating that the deletion of this segment (segment 4 and part of segment 3 in domain III attributed to alternative deletion of exon 20) might be responsible for the lack of currents associated with CbmNav1.7b (Fig. 3F–H). $Na^+$ currents were recorded from mutants 5 and 6, but not mutant 4 (Fig. 3I–K). In contrast, $Na^+$ currents were recorded from mutant 7 but not mutants 8 and 9 (Fig. 3L–N). This suggested that an amino-acid substitution (C934R) located in the extracellular linker between segments 5 and 6 of domain II might be the key factor leading to loss of currents in CbmNav1.7a and 1.7b. Furthermore, western blot and immunolabeling experiments showed that Nav1.7 protein was present in the membrane and cytosol of HEK293T cells transfected with mutant 4, suggesting that the residue replacement C934R results in complete loss-of-function of Nav1.7 (Fig. S3).

Then, we speculated that the $Na^+$ currents of hair cells might be attributable to functional CbmNav1.7a$_{(C934)}$ (mutant 7) under physiological conditions. To test this hypothesis, we compared the biophysical properties of wtNav1.7 and CbmNav1.7a$_{(C934)}$. The expression levels of the two variants were not statistically different with a current density of 384.03 ± 44.63 pA/pF for wtNav1.7 ($n = 20$) and 320.54 ± 58.2 pA/pF for CbmNav1.7a$_{(C934)}$ ($n = 15$), and their peak currents were observed at − 10 mV (Fig. 4A). There was no significant difference between wtNav1.7 and CbmNav1.7a$_{(C934)}$ in terms of the $G(V)$ relationship and the recovery process (Fig. 4B, H and Table 2). The fast inactivation time constants in the range of depolarization (− 20 mV to + 20 mV) of CbmNav1.7a$_{(C934)}$ were significantly larger ($P < 0.001$) (Fig. 4C). The midpoint of activation ($V_{1/2}$) for steady-state inactivation of CbmNav1.7a$_{(C934)}$ was significantly shifted leftward ($P < 0.001$), while the slope factor ($k_m$) remained unchanged (Fig. 4D, Table 2). The $V_{1/2}$ of fast inactivation for CbmNav1.7a$_{(C934)}$ was shifted in a hyperpolarizing direction ($P < 0.05$), whereas the $k_m$ remained unchanged (Fig. 4E, Table 2). The time constants for deactivation of CbmNav1.7a$_{(C934)}$ during potentials ranging from − 100 mV to + 40 mV were smaller ($P < 0.001$) (Fig. 4F). In addition, the peak amplitude of the ramp current of CbmNav1.7a$_{(C934)}$ was significantly larger than that of wtNav1.7 ($P < 0.05$) (Fig. 4G). The recovery time constant and $I_{max}$ of CbmNav1.7a$_{(C934)}$ were similar to those of wtNav1.7 (Fig. 4H, Table 2). These data showed that CbmNav1.7a$_{(C934)}$ was associated with a slower fast-inactivation process from the open-state and a quicker deactivation process as well as a larger ramp current amplitude.

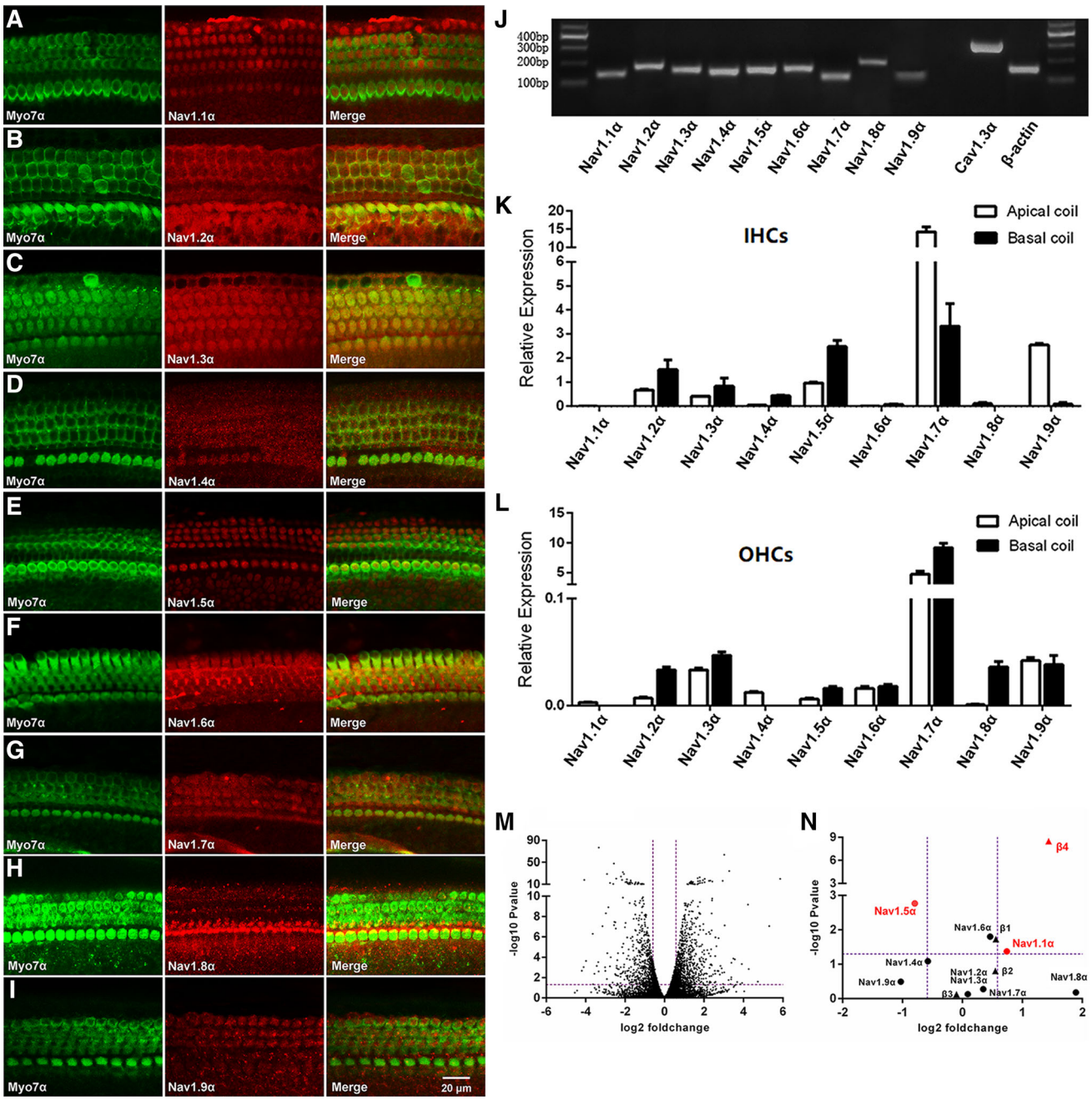


**Fig. 2** Distribution and expression of VGSC subtypes in immature hair cells. **A–I** Red, VGSC subtypes (anti-Nav1.1α–1.9α); green, hair cell specific–marker (anti-myosin 7α); yellow, co-labeling. **J** mRNA segments of the 9 VGSC α subunits from sensory epithelia. **K, L** mRNA expression levels of Nav1.1α–1.9α in single IHCs and OHCs in apical and basal sensory epithelia from P6 mice. **M** Volcano plots of the expression levels of genes in apical and basal sensory epithelia (y-axis, $\log_{10}$ *P*-value of difference; x-axis, $\log_2$ fold-changes; fold-change $\geq 1.5$ and *P*-value $< 0.05$ were set as threshold to identify differentially-expressed genes). **N** *P* values *vs* fold-changes for the 9 α-subunits and 4 β-subunits of VGSCs; red, differentially-expressed genes (Nav1.1α, 1.5α, and β4).

### Alternative Splicing Events Modified the Characteristics of CbmNav1.7a$_{(C934)}$

To determine whether alternative splicing events contribute to the function of CbmNav1.7a$_{(C934)}$, the biophysical properties of wtNav1.7, mutant 1, and mutant 2 were compared. Mutant 1 did not significantly differ from wtNav1.7 in terms of *I–V* curve (348.25 ± 52.5 pA/pF for mutant 1 at − 10 mV, $n = 10$), *G*(*V*) relationship, $V_{1/2}$ and $k_m$ of steady-state inactivation and fast inactivation, and recovery time constants (Fig. 5A, B, D, H, Table 3). Analyses of current decay showed that the $\tau_{fast}$ and $\tau_{slow}$ of

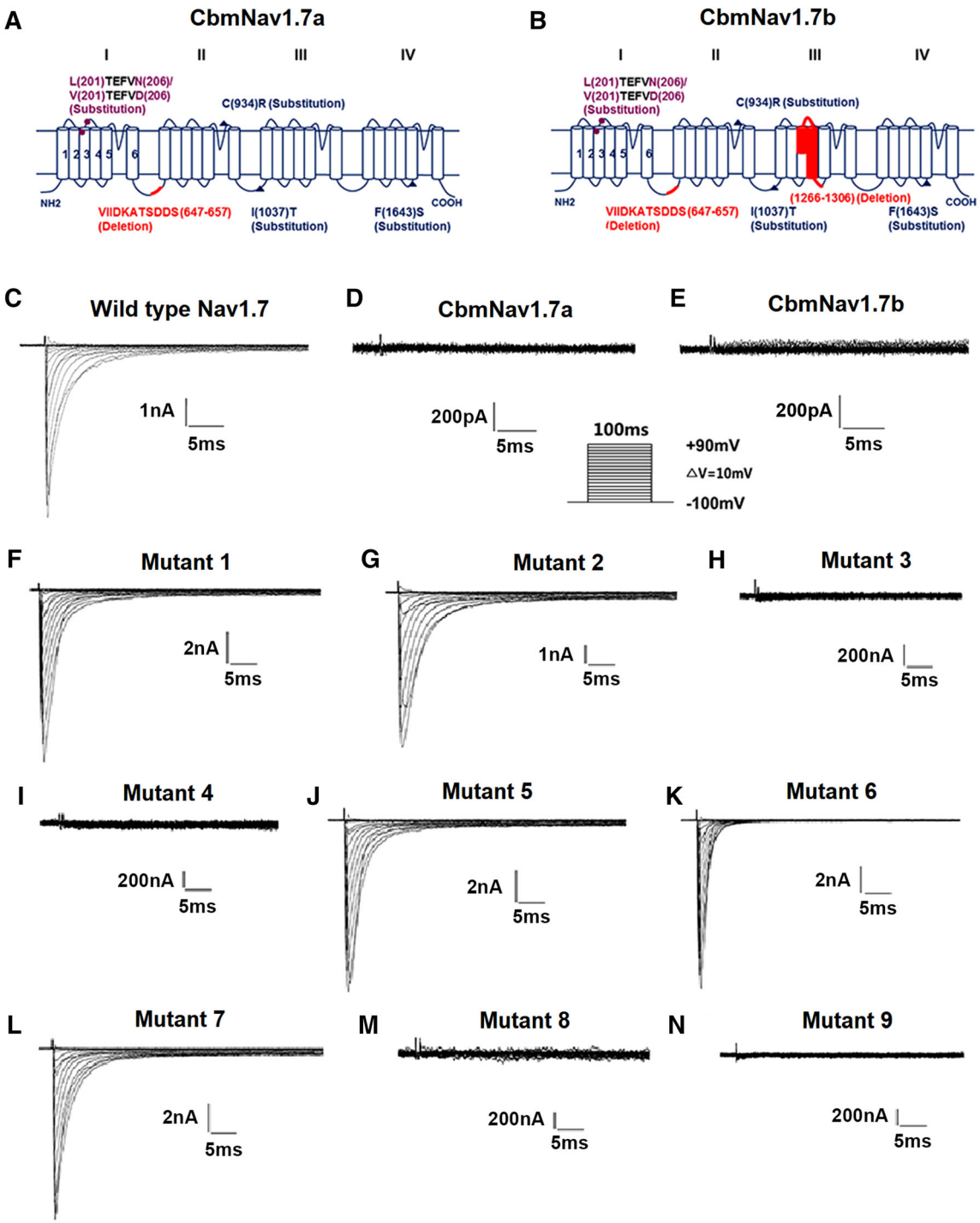


**Fig. 3** Electrophysiological recordings from CbmNav1.7 variants and related mutants in HEK293T cells. **A, B** Locations of the substitution and deletion of amino-acids in CbmNav1.7a and 1.7b compared with wtNav1.7 (purple, segment replacement generated by alternative splicing of exon 5; red, segment deletion generated by alternative splicing of exon 11 or exon 20; blue, single amino-acid residue replacement produced by three RNA editing events in exons 15, 16. and 26). **C–E** $Na^+$ current recordings from wtNav1.7, CbmNav1.7a, and CbmNav1.7b exogenously expressed in HEK293T cells. **F–N** $Na^+$ current recordings of nine Nav1.7 mutants exogenously expressed in HEK293T cells.

mutant 1 were both smaller than those of wtNav1.7 ($P < 0.001$ and $P < 0.01$, respectively) at high depolarizing voltages (0 mV to 20 mV), whereas $\tau_{fast}$ was markedly larger ($P < 0.05$) at low depolarizing voltages (− 20 mV to − 10 mV) (Fig. 5C). Analyses of deactivation kinetics showed that the time constant of deactivation for mutant 1

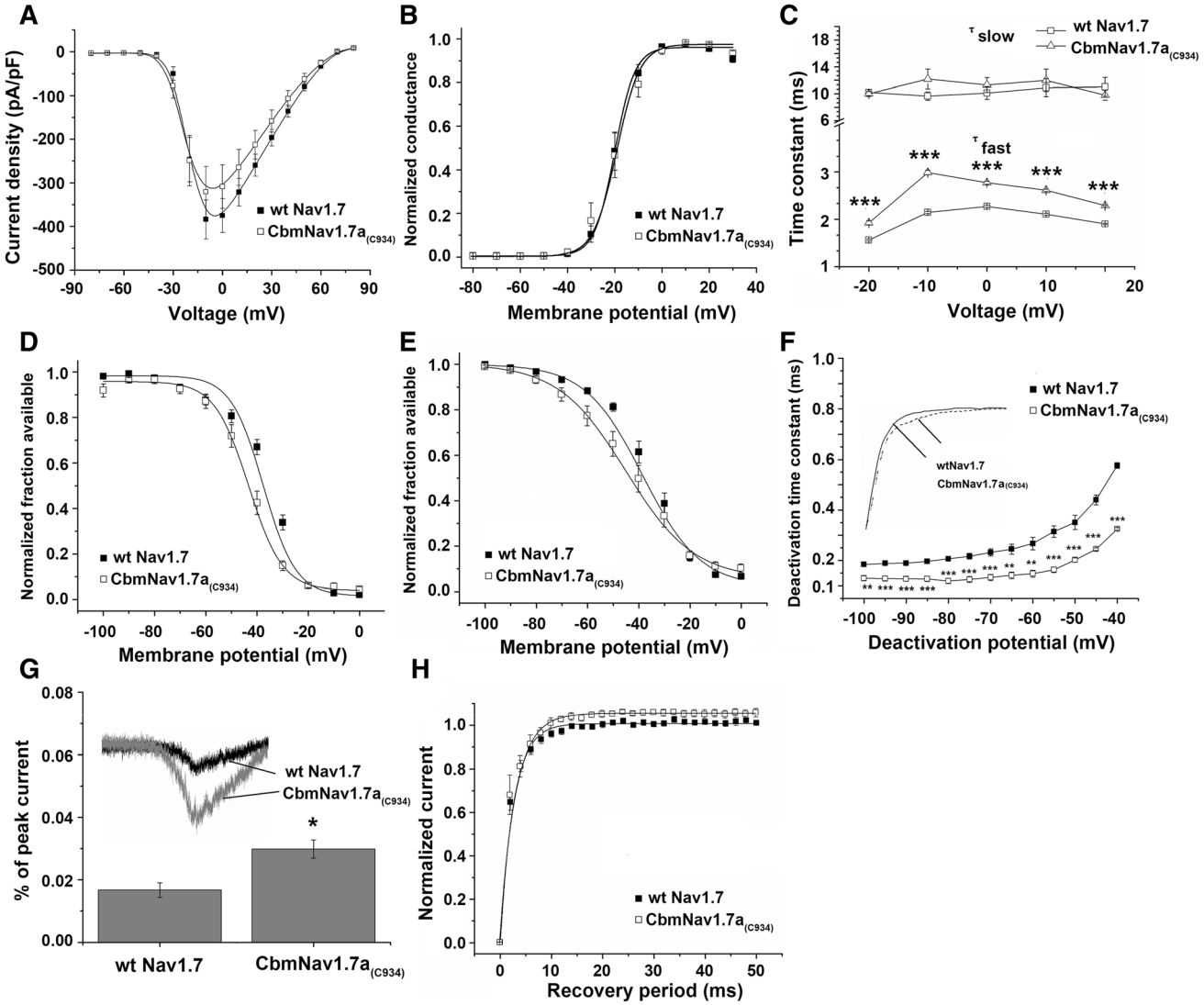


**Fig. 4** Biophysical properties of CbmNav1.7a$_{(C934)}$. **A** Peak current-voltage relationships for wtNav1.7 (black squares) and CbmNav1.7a$_{(C934)}$ (white squares). **B** Voltage-dependence of activation of wtNav1.7 and CbmNav1.7a$_{(C934)}$ fitted with a Boltzmann function. **C** Kinetics of inactivation of wtNav1.7 (white squares) and CbmNav1.7a$_{(C934)}$ (white triangles) fitted with a double-exponential equation, and the time constants representing the slow ($\tau_{slow}$) and fast ($\tau_{fast}$) components. **D** Voltage-dependence of steady-state inactivation of wtNav1.7 (black squares) and CbmNav1.7a$_{(C934)}$ (white squares) fitted with a Boltzmann function. **E** Voltage-dependence of fast inactivation of wtNav1.7 and CbmNav1.7a$_{(C934)}$ fitted with a Boltzmann function. **F** Time constant for tail current deactivation at repolarization potentials ranging from − 100 to − 40 mV for wtNav1.7 and CbmNav1.7a$_{(C934)}$ obtained with single-exponential fits. **G** Example of ramp current traces for wtNav1.7 (black line) and CbmNav1.7a$_{(C934)}$ (grey line); peak ramp currents were calculated. **H** Recovery of channel availability from fast inactivation of wtNav1.7 and CbmNav1.7a$_{(C934)}$; the continuous curve is a single-exponential function fitted to the data with a time constant. $^{*}P < 0.05$, $^{**}P < 0.01$, $^{***}P < 0.001$, wtNav1.7 *vs* CbmNav1.7a$_{(C934)}$, unpaired Student's *t*-test. Data are presented as the mean ± SEM.

was significantly larger ($P < 0.01$) than wtNav1.7 across a range of voltages from − 100 mV to − 80 mV (Fig. 5F). In addition, mutant 1 also had a larger peak value of ramp current than wtNav1.7 ($P < 0.05$) (Fig. 5G). These data signified that the alternative splicing of exon 5, leading to amino-acid replacements L201V/N206D, accelerates the fast/slow inactivation at high depolarizing voltages, retards the fast inactivation at low depolarizing voltages, slows the deactivation, and increases the ramp current.

Mutant 2 did not differ significantly from mutant 1 in terms of *I-V* curve (373.82 ± 53.6 pA/pF for mutant 2 at 0 mV, $n = 14$), $G(V)$ relationship, $V_{1/2}$ and $k_m$ of steady-state inactivation and fast inactivation, recovery time constant, and ramp current (Fig. 5A, B, D–H, Table 3). The $\tau_{fast}$ of mutant 2 was significantly larger at higher depolarizing potentials (0 mV to 20 mV) ($P < 0.001$) (Fig. 5C) and its deactivation time constant was lower for potentials ranging from − 100 mV to − 40 mV

**Table 2** Biophysical properties of CbmNav1.7a$_{(C934)}$ variant.

| Mutant form | Voltage-dependent activation | | | Steady-state inactivation | | |
|---|---|---|---|---|---|---|
| | $V_{1/2}$ (mV) | $k_m$ (mV) | $n$ | $V_{1/2}$ (mV) | $k_m$ (mV) | $n$ |
| wtNav1.7 | − 20.00 ± 1.64 | 4.23 ± 0.55 | 19 | − 37.53 ± 1.61 | 6.31 ± 0.82 | 9 |
| CbmNav1.7a$_{(C934)}$ | − 19.13 ± 2.25 | 4.89 ± 0.90 | 14 | − 43.26 ± 0.85*** | 6.63 ± 0.52 | 8 |
| Mutant form | Fast inactivation | | | Recovery from inactivation | | |
| | $V_{1/2}$ (mV) | Time (ms) | $n$ | $I_{max}$ | Time (ms) | $n$ |
| wtNav1.7 | − 38.45 ± 2.27 | 11.24 ± 1.11 | 9 | 1.00 ± 0.004 | 2.61 ± 0.14 | 8 |
| CbmNav1.7a$_{(C934)}$ | − 44.83 ± 1.51* | 13.22 ± 1.05 | 14 | 1.05 ± 0.002 | 3.02 ± 0.11 | 6 |

Note: Values are mean ± SEM

*Significant difference (*$P < 0.05$, ***$P < 0.001$) between wtNav1.7 and CbmNav1.7a$_{(C934)}$ using unpaired Student's two-tailed *t*-test.

($P < 0.01$) (Fig. 5F). These data indicated that the alternative splicing of exon 11, leading to a deletion of amino-acid fragment 647–657, slows the fast inactivation at high potentials and accelerates the deactivation.

The $\tau_{fast}$ of mutant 2 across potentials from − 20 mV to 20 mV was significantly larger than that of wtNav1.7 ($P < 0.05$), while the $\tau_{slow}$ at 10 mV was smaller ($P < 0.01$) (Fig. 5C). The deactivation time constant was markedly smaller than that of wtNav1.7 (− 40 mV to − 100 mV) ($P < 0.05$) (Fig. 5F), and the peak ramp current of mutant 2 was also larger than that of wtNav1.7 ($P < 0.05$) (Fig. 5G).

### RNA Editing Events Account for the Functional Characteristics of CbmNav1.7a$_{(C934)}$

To investigate whether RNA editing events contribute to the function of CbmNav1.7a$_{(C934)}$, we broadly compared its biophysical properties with those of mutants 2, 5, and 6. We found no significant differences between mutants 2 and 5 in terms of *I-V* curve (376.28 ± 84.17 pA/pF for mutant 5 at − 10 mV, $n = 7$), $G(V)$ relationship, $V_{1/2}$ and $k_m$ of steady-state inactivation and fast inactivation, ramp current, and recovery (Fig. 6A, B, D, E, G, H, Table 4). Compared to mutant 2, the $\tau_{fast}$ of mutant 5 was larger for potentials from − 20 mV to 20 mV ($P < 0.01$), whereas the $\tau_{slow}$ showed selective increases at some depolarizing potentials ($P < 0.01$) (Fig. 6C). The deactivation time constant of mutant 5 was higher at − 40 mV and − 45 mV ($P < 0.05$) (Fig. 6F). These results show that the U-to-C RNA editing at exon 16, leading to the amino-acid substitution I1037T, delays fast/slow inactivation, and deactivation.

The current density (310.54 ± 32.93 pA/pF for mutant 6 at − 10 mV, $n = 11$), $G(V)$ relationship, recovery, and ramp current for mutants 2 and 6 did not statistically differ (Fig. 6A, B, G, H, Table 4). The $\tau_{fast}$ of mutant 6 was significant smaller for potentials from − 20 mV to 20 mV ($P < 0.05$) (Fig. 6C). The steady-state and fast inactivation curves of mutant 6 were both shifted in a hyperpolarizing direction, and their $V_{1/2}$ values were each decreased ($P < 0.001$) (Fig. 6D, E, Table 4). In addition, the deactivation time constant was markedly larger than that of mutant 2 for potentials from − 100 mV to − 40 mV ($P < 0.001$) (Fig. 6F). These data indicate that the U-to-C RNA editing at exon 26, leading to the amino-acid substitution F1643S, accelerates fast inactivation, delays the transition of the channel from an inactive to an open state, and delays deactivation.

The $\tau_{fast}$ of CbmNav1.7a$_{(C934)}$ was larger for potentials from − 10 mV to 20 mV than mutant 2 ($P < 0.001$) (Fig. 6C). The steady-state and fast inactivation curves for CbmNav1.7a$_{(C934)}$ were both shifted in a hyperpolarizing direction, and their $V_{1/2}$ values were each decreased ($P < 0.001$ and $P < 0.05$) (Fig. 6D, E and Table 4). These data suggested that the two RNA editing events cooperatively slow the fast inactivation and delay the transition from an inactive to an open state.

## Discussion

### Physiological Role of Sodium Currents in Pre-hearing Hair Cells

Spontaneous electrical activity is a common feature of sensory systems during early development, and has been implicated in promoting neural survival and maturation, as well as the growth and refinement of their projections to yield circuits [20–23]. In the auditory system, spontaneous electrical activity generated by cochlear hair cells before the onset of hearing has also been implicated in shaping the

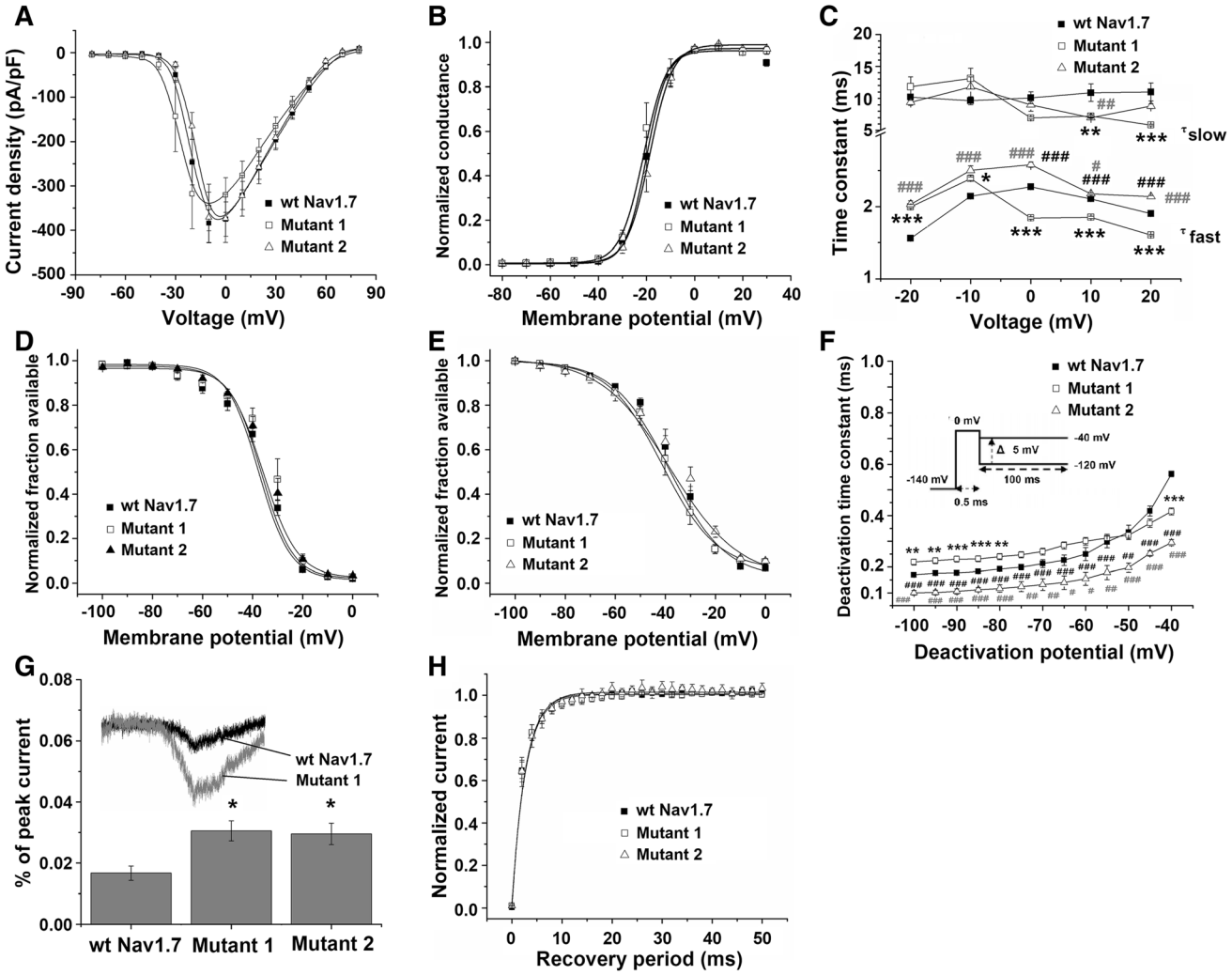


**Fig. 5** Biophysical properties of alternative splicing variants of CbmNav1.7a. **A** Peak current-voltage relationships of wtNav1.7, mutant 1, and mutant 2. **B** Voltage-dependence of activation of wtNav1.7, mutant 1, and mutant 2 fitted with a Boltzmann function. **C** Kinetics of inactivation of wtNav1.7, mutant 1 and mutant 2 fitted with a double-exponential equation, and the time constants representing the slow ($\tau_{slow}$) and fast ($\tau_{fast}$) components. Symbols: wtNav1.7 (black squares), mutant 1 (white squares), mutant 2 (white triangles). **D** Voltage-dependence of steady-state inactivation of the 3 variants fitted with a Boltzmann function. **E** Voltage-dependence of fast inactivation of the 3 variants fitted with a Boltzmann function. **F** Time constant for tail current deactivation at repolarization potentials ranging from − 100 to − 40 mV for the 3 variants, obtained from single-exponential fits. *Difference between wtNav1.7 and mutant 1; #(dark), difference between mutants 1 and 2; #(gray), difference between wtNav1.7 and mutant 2. **G** Example of ramp current traces for wtNav1.7 (black) and mutant 1 (grey); peak ramp currents were calculated, *significant difference of mutant 1 and mutant 2 each compared with wtNav1.7. **H** Recovery of channel availability from fast inactivation of the 3 variants; continuous curve is a single-exponential function fitted to the data with a time constant. $*P < 0.05$, $**P < 0.01$, $***P < 0.001$, one-way ANOVA followed by a Bonferroni *post-hoc* test for multiple comparison of the wtNav1.7, mutant1 and mutant 2. Data are presented as the mean ± SEM.

organization of nascent circuits [24, 25]. The spontaneous action potentials in premature IHCs are mainly due to the interplay between an inward $Ca^{2+}$ current and a delayed rectifier $K^+$ current and are also finely modulated by other transiently-occurring conductance events, such as small conductance $Ca^{2+}$-sensitive $K^+$ currents [5]. In this study, we found that the spontaneous action potentials in premature IHCs were reversibly abolished by $Ca^{2+}$-free solution, clearly showing that spontaneous activity is $Ca^{2+}$-dependent, consistent with a previous report [8]. The typical inward $Na^+$ current was recorded in IHCs from P6 mice, and the biophysical characteristics were similar to those in premature rat IHCs [17]. However, although it is the main contributor to the rising phase of the action potential in most neurons [12], the $Na^+$ current in immature IHCs is not necessary for the generation of action potentials, but rather regulates their frequency [8]. In the present study, we re-assessed the potential

**Table 3** Biophysical properties of mutant 1 and mutant 2.

| Mutant form | Voltage-dependent activation | | | Steady-state inactivation | | |
|---|---|---|---|---|---|---|
| | $V_{1/2}$ (mV) | $k_m$ (mV) | $n$ | $V_{1/2}$ (mV) | $k_m$ (mV) | $n$ |
| wtNav1.7 | − 20.00 ± 1.64 | 4.23 ± 0.55 | 19 | − 37.53 ± 1.61 | 6.31 ± 0.82 | 9 |
| Mutant 1 | − 21.28 ± 1.29 | 4.76 ± 0.51 | 11 | − 37.37 ± 1.78 | 6.65 ± 0.88 | 8 |
| Mutant 2 | − 18.65 ± 1.22 | 4.69 ± 0.51 | 14 | − 35.84 ± 1.16 | 6.86 ± 0.62 | 10 |
| Mutant form | Fast inactivation | | | Recovery from inactivation | | |
| | $V_{1/2}$ (mV) | $k_m$ (mV) | $n$ | $I_{max}$ | Time (ms) | $n$ |
| wtNav1.7 | − 38.45 ± 2.27 | 11.24 ± 1.11 | 9 | 1.00 ± 0.004 | 2.61 ± 0.14 | 8 |
| Mutant 1 | − 40.95 ± 1.61 | 10.83±0.88 | 6 | 0.99 ± 0.002 | 2.70 ± 0.14 | 5 |
| Mutant 2 | − 38.02 ± 2.81 | 13.76 ± 1.74 | 8 | 1.00 ± 0.004 | 2.71 ± 0.16 | 8 |

Note: Values are mean ± SEM. No significant difference between wtNav1.7, mutant 1 and mutant 2 using one-way ANVOA followed by a Bonferroni *post-hoc* test.

physiological role of $Na^+$ current in immature IHCs and found that it shaped their action potentials by decreasing the time necessary for the membrane potential to reach a threshold. These data strongly suggest that the $Na^+$ current can make the generation of spontaneous action potentials in immature IHCs more robust and regulate their frequency.

On the other hand, our current recordings showed that premature OHCs did not fire spontaneous action potentials, although a single action potential was triggered by depolarizing current injection from the resting potential, in accord with a previous study [26]. Since IHCs and OHCs exhibit otherwise qualitatively similar basolateral membrane currents, the lack of repetitive action potential activity in OHCs is somewhat surprising. This might be due to the absence of the SK2 current, which plays a crucial role in sustaining repetitive action potential activity in immature IHCs, and/or different concentrations of $Ca^{2+}$-buffering proteins between the two cell types [27, 28]. In addition, Cav1.3 gene knockout induces the degeneration of OHCs as well as IHCs, pointing to a possible role of $Ca^{2+}$ action potentials in the normal maturation of both immature hair cell types [29]. The typical $Na^+$ current was initially recorded in premature OHCs from isolated acute cochlear sensory epithelia in the present study, which verified the existence of a $Na^+$ current in isolated premature OHCs [10]. The $Na^+$ current in early developmental stage strongly suggests a noteworthy role in OHC maturation.

## Composition of VGSC Subunits in Pre-hearing Hair Cells

The $Na^+$ currents in premature cochlear IHCs and OHCs are considered to be TTX-sensitive [8, 10]. Nav1.1α and Nav1.6α have been determined to be located on the membrane of IHCs and OHCs, whereas Nav1.2α and Nav1.7α are located on the nerve fibers below IHCs and OHCs [17]. In the current study, we found six VGSC subtypes (Nav1.1α, 1.2α, 1.3α, 1.4α, 1.6α, and 1.7α) mediating TTX-sensitive currents on the membrane of IHCs and OHCs, which strongly hinted that multiple subtypes might synergistically contribute to the $Na^+$ currents in developing hair cells. Furthermore, three subtypes (Nav1.5α, 1.8α, and 1.9α) that mediate TTX-insensitive currents were also detected in premature IHCs and OHCs. These results are consistent with previous findings identifying the full-length mRNA encoding nine VGSC subtypes in developing cochlear sensory epithelia [18]. However, it seems that the three subtypes with extremely low abundance (Nav1.5α, 1.8α, and 1.9α) cannot functionally mediate the detectable TTX-insensitive currents in immature hair cells [8, 17]. Furthermore, the biophysical properties of $Na^+$ currents in IHCs and OHCs are similar, but their sensitivity to TTX differs (1 mmol/L TTX fully blocks the currents in IHCs, while 10 mmol/L is required for OHCs) [10, 17]. This discrepancy could be attributed to the combinational expression patterns and the expression levels of VGSC subtypes in the two types of hair cell.

Among the nine known subtypes of VGSC, the Nav1.7 subtype has been suggested to be the main carrier of $Na^+$ currents in premature IHCs, because of the similarity in its biophysical and pharmacological properties [8]. Nav1.7 is preferentially expressed in peripheral neurons and produces a TTX-sensitive $Na^+$ current with hyperpolarized steady-state activation/inactivation, and fast kinetics [30]. The interesting thing is that the biophysical properties, channel kinetic characteristics, and the pharmacological sensitivity to TTX ($K_D$ 4.8 ± 0.6 nmol/L) of $Na^+$ current in immature IHCs were similar to that carried by Nav1.7 ($K_D$ of TTX

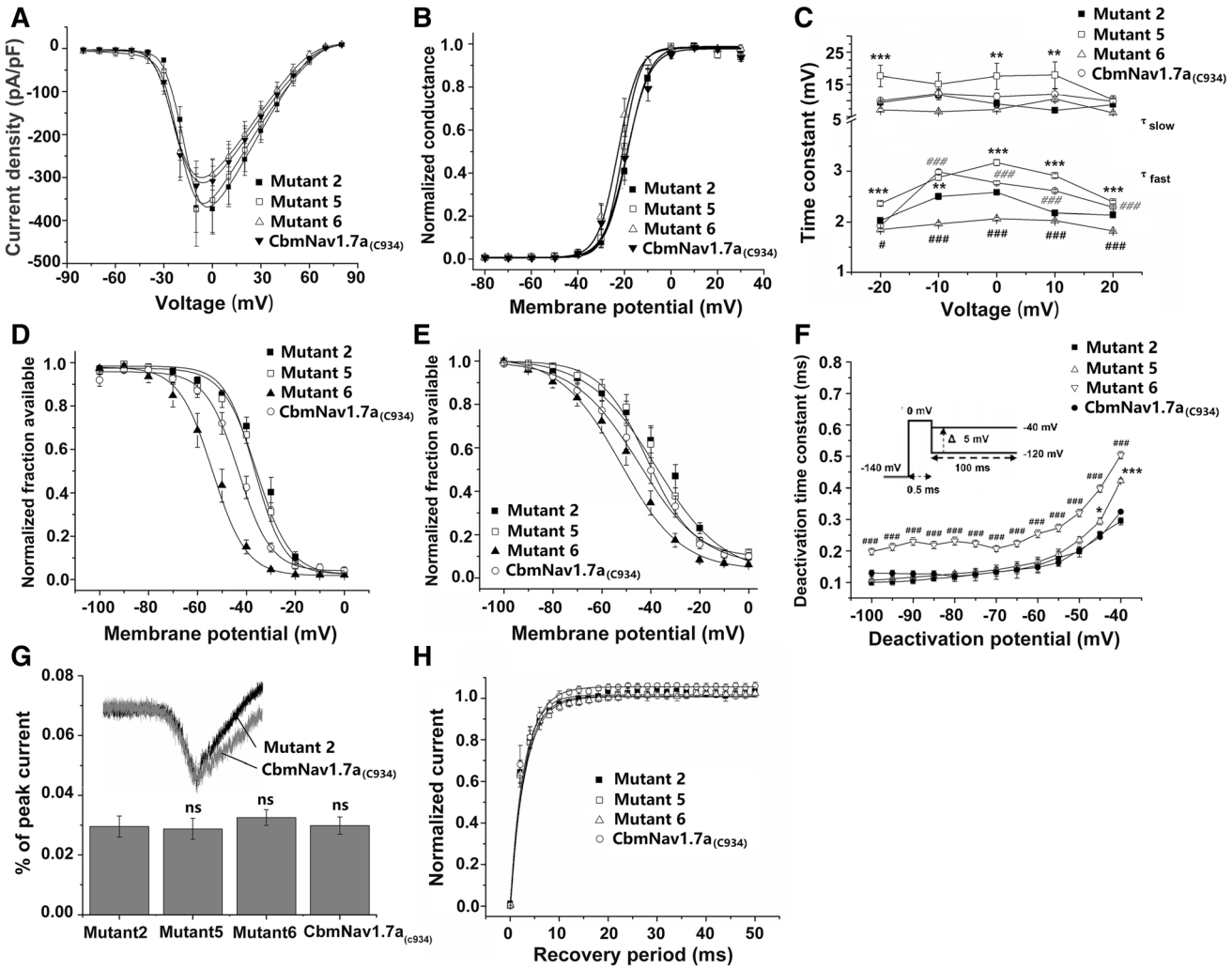


**Fig. 6** Biophysical properties of RNA editing variants of CbmNav1.7a. **A** Peak current-voltage relationships of mutants 2, 5, 6, and 7 (CbmNav1.7a$_{(C934)}$). **B** Voltage-dependence of activation of the variants fitted with a Boltzmann function. **C** Kinetics of inactivation of the variants with a double-exponential equation, and the time constants representing the slow ($\tau_{slow}$) and fast ($\tau_{fast}$) components. *difference between mutants 2 and 5; #(dark), difference between mutants 2 and 6; #(gray), difference between mutant 2 and CbmNav1.7a$_{(934)}$. **D** Voltage-dependence of steady-state inactivation of the variants fitted with a Boltzmann function. **E** Voltage-dependence of fast inactivation of the variants fitted with a Boltzmann function. **F** Time constants for tail current deactivation at repolarization potentials ranging from − 100 to − 40 mV for the variants from single-exponential fits. **G** Example of ramp current traces for mutant 2 (black) and CbmNav1.7a$_{(C934)}$ (grey); the peak ramp currents were calculated. **H** Recovery of channel availability from fast inactivation of the variants; the continuous curve is a single-exponential function fitted to the data with a time constant. *$P < 0.05$, **$P < 0.01$, ***$P < 0.001$, one-way ANOVA followed by a Bonferroni *post-hoc* test for multiple comparisons of the variants. Data are presented as the mean ± SEM.

4.3 ± 0.92 nmol/L) [8, 17]. In the present study, we showed that Nav1.7 protein was located on the membrane of hair cells and was also the predominant $Na^+$ channel transcript in single hair cells, with low abundance of other $Na^+$ channel transcripts. In our previous work, Nav1.6α mRNA was shown to have higher expression levels than the other eight subtypes in developing sensory epithelia [18]; however, the single-cell qPCR data here showed that the mRNA expression level of Nav1.6α was markedly lower than that of Nav1.7α in single hair cells. These inconsistent results may be due to the different experimental material used. The cochlear sensory epithelia used in the previous study consisted of many types of cells (hair cells, supporting Deiters' cells, Hensen cells, pillar, inner phalangeal, and border cells), and Nav1.6α might have been expressed not only in hair cells but also in other subtypes in the immature cochlea. These findings led us to hypothesize that Nav1.7 is the main contributor to the $Na^+$ current in immature hair cells. In addition, Nav1.7 generates currents with slow closed-state inactivation that permits the production of ramp currents in response to small, slow depolarization near the resting membrane

**Table 4** Biophysical properties of mutant 5 and mutant 6.

| Mutant form | Voltage-dependent activation | | | Steady-state inactivation | | |
|---|---|---|---|---|---|---|
| | $V_{1/2}$ (mV) | $k_m$ (mV) | $n$ | $V_{1/2}$ (mV) | $k_m$ (mV) | $n$ |
| Mutant 2 | − 18.65 ± 1.22 | 4.69 ± 0.51 | 14 | − 35.84 ± 1.16 | 6.86 ± 0.62 | 10 |
| Mutant 5 | − 20.90 ± 1.55 | 3.77 ± 0.77 | 8 | − 36.05 ± 1.21 | 5.86 ± 0.64 | 6 |
| Mutant 6 | − 21.54 ± 0.67 | 4.60 ± 0.25 | 12 | − 54.99 ± 1.01*** | 7.08 ± 0.46 | 9 |
| CbmNav1.7a $_{(C934)}$ | − 19.13 ± 2.25 | 4.89 ± 0.90 | 14 | − 43.26 ± 0.85*** | 6.63 ± 0.52 | 8 |

| Mutant form | Fast inactivation | | | Recovery from inactivation | | |
|---|---|---|---|---|---|---|
| | $V_{1/2}$ (mV) | $k_m$ (mV) | $n$ | $I_{max}$ | Time (ms) | $n$ |
| Mutant 2 | − 38.02 ± 2.81 | 13.76 ± 1.74 | 8 | 1.00 ± 0.004 | 2.71 ± 0.16 | 8 |
| Mutant 5 | − 41.63 ± 1.65 | 9.50 ± 0.89 | 8 | 1.01 ± 0.003 | 3.05 ± 0.13 | 4 |
| Mutant 6 | − 52.26 ± 1.78 *** | 12.41 ± 1.25 | 9 | 1.01 ± 0.003 | 2.87 ± 0.10 | 6 |
| CbmNav1.7a $_{(C934)}$ | − 44.83 ± 1.51* | 13.22 ± 1.05 | 14 | 1.05 ± 0.002 | 3.02 ± 0.11 | 6 |

Note: Values are mean ± SEM.

*Significant difference (* $P < 0.05$, *** $P < 0.001$) of mutant 2 vs mutant 6, and mutant2 *versus* CbmNav1.7a $_{(C934)}$ using one-way ANVOA followed by a Bonferroni *post-hoc* test.

potential [31]. Thus, Nav1.7 could be a threshold channel that amplifies small membrane depolarization close to the action potential threshold [32]. For example, in peripheral DRG neurons, the shape of the action potential is determined mainly by TTX-resistant $Na^+$ currents, but Nav1.7 current contributes to the spike waveform by decreasing the time to reach threshold [33]. This might allow the conclusion that the $Na^+$ currents mainly carried by Nav1.7 contribute to the subthreshold depolarization and regulate the frequency of spontaneous action potentials in premature hair cells.

It is known that the primary α-subunit forms the central pore of the VGSC and serves as the voltage sensor, while the auxiliary β-subunits modulate the gating kinetics and surface expression of VGSCs [34]. Here, we demonstrated that four β-subunits (β1–β4) are expressed in immature sensory epithelia, the β4 subunit being highly expressed in basal sensory epithelia. These details raise an interesting question, specifically whether α and β subunits of VGSCs assemble in a dynamic matched-paired formation in apical and basal sensory epithelia.

## Post-transcriptional Regulation of VGSCs in Developing Cochlea

Transcriptional modification events such as alternative splicing and RNA editing result in a single gene encoding multiple functional proteins. VGSCs undergo extensive transcriptional modification under various physiological and pathological conditions. Our previous study has shown that two novel Nav1.7 variants (CbmNav1.7a and 1.7b) in cochlear sensory epithelia undergo various post-transcriptional modifications [18]. The interesting question is whether the cochlea-specific modifications affect the gating properties and kinetic parameters of Nav1.7. In the present study, the $Na^+$ currents of CbmNav1.7a and 1.7b could not be detected in HEK293T cells. The $Na^+$ current recordings from eight Nav1.7 mutants revealed that the disappearance of CbmNav1.7a currents was attributable to an amino-acid residue replacement (C934R) located at the extracellular linker between segments 5 and 6 of domain II *via* U-to-C RNA editing in exon 15. In this case, the uncharged Cys residue was replaced by a positively-charged Arg residue, which led to the loss of the CbmNav1.7a current. If so, $Cys/Arg_{934}$ might be a novel loss-of-function mutation in Nav1.7 that occurs under physiological conditions. Moreover, the lack of segment 4 and part of segment 3 in domain III of CbmNav1.7b results in a truncated non-functional channel protein. A somewhat similar modification event has been shown in the *hNav1.6* and *CACNL1A4* genes, and this was speculated to be a "fail-safe" mechanism [35, 36]. These data suggest that the RNA editing in exon 15 and alternative splicing of exon 20 could result in "fail-safe" protection of CbmNav1.7 in premature hair cells, which might be beneficial for decreasing cellular excitability under physiological conditions.

The next question concerns which Nav1.7 variant is the main contributor to $Na^+$ currents in cochlear hair cells *in vivo*. Here, we considered CbmNav1.7a$_{(C934)}$ to be a potential candidate. Compared to wtNav1.7, the functional shift of CbmNav1.7a$_{(C934)}$ (slower fast-inactivation from open-state, faster deactivation, and larger ramp current) could strengthen its ability to receive and amplify weak electrical signals under conditions of lower depolarized membrane voltage. These results imply that the $Na^+$ currents in developing IHCs might be attributed to

**Table 5** Respective contributions of transcriptional modification events for biophysical properties of CbmNav1.7a$_{(C934)}$.

| Location sites | Exon 5 | Exon 11 | Exon 5&11 | Exon 16 | Exon 26 | Exon 16&26 | Altered properties of CbmNa1.7a$_{(C934)}$ |
|---|---|---|---|---|---|---|---|
| Posttranscriptional modification events | Alternative splicing | Alternative splicing | | RNA editing | RNA editing | | |
| Amino acid substitution or deletion | L201V/N206D | 647–657 deletion | L201V/ N206D 647–657 deletion | I1037T | F1643S | I1037T& F1643S | |
| Topological structure | Extracellular linker of S3 and S4 in Domain I | Intracellular linker of Domain I and II | | Intracellular linker of Domain II and III | Intracellular linker of S4 and S5 in Domain IV | | |
| Channel dynamics | | | | | | | |
| Activation | | | | | | | |
| Inactivation component | + | − | − | − | + | − | − |
| Steady inactivation | | | | | − | − | − |
| Fast inactivation | | | | | − | − | − |
| Deactivation | − | + | + | | − | | + |
| Ramp current | + | | + | | | | + |

Note:"+" represents the process is faster or larger, "−" represents the process is slower, "empty form" represents no change.

CbmNav1.7a$_{(C934)}$ *in vivo*, which is largely activated around the resting membrane potential and then involved in shaping spontaneous action potentials.

Finally, it was unclear which post-transcriptional events lead to the distinctive biophysical properties of CbmNav1.7a$_{(C934)}$. The ramp current of CbmNav1.7a$_{(C934)}$ was increased by (201)V(206)D (exon 5 alternative splicing) in the DI/S3–S4 linker. This result was in accord with a previous report showing that exon 5 (5N and 5A) alternative splicing of *hNav1.7* enhances the amplitude of currents in response to a slowly-depolarizing ramp stimulus [37]. The faster deactivation associated with CbmNav1.7a$_{(C934)}$ was attributed to deletion of the 647–657 amino-acid fragment (exon 11 alternative splicing). In addition, F1643S (a U-to-C RNA editing event in exon 26) delayed the deactivation process, and I1037T itself had no effect on deactivation. The delayed inactivation from the open state in CbmNav1.7a$_{(C934)}$ might be induced by the systemic roles of the two alternative splicing events and two RNA editing events noted above, and the accelerated deactivation of CbmNav1.7a$_{(C934)}$ might be attributed to two alternative splicing events and an RNA editing event at exon 26. These results indicate that the residue replacements and fragment deficiency distributed in four functional areas can modify channel dynamics in an individual or combinational manner (Table 5).

It was also interesting that deactivation of the Nav1.7 variant was delayed by the F1643S substitution; however, when I1037T coexisted with F1643S, the deactivation was conserved. The I1037T substitution was located at the intracellular linker between DII and DIII of CbmNav1.7a$_{(C934)}$, whereas the F1643S substitution was at the intracellular linker between DIV S4 and DIV S5. One remaining question is how these two modifications regulate the deactivation of CbmNav1.7a$_{(C934)}$. Regardless, these results provide important clues to understanding the dynamic-functional mechanisms of VGSCs.

## Conclusion

The present study demonstrated that cochlea-specific post-transcriptional modifications amend the biophysical properties of the CbmNav1.7 variant, the main contributor to $Na^+$ currents involved in regulating the frequency of spontaneous action potentials in premature IHCs.

**Acknowledgements** We thank Prof. Lin Chen (University of Science and Technology of China) and Dr. Juanmei Yang (Eye and ENT Hospital of Fudan University) for valuable help with cochlear microscopic anatomy. This work was supported by the National Natural Science Foundation of China (31571032, 31771191, and 81730028), the National Basic Research Development Program of China (SQ2017YFSF080012), and the Postdoctoral Science Foundation of China (2018M640407).

**Conflict of interest** All authors claim that there are no conflicts of interest.

## References


1. Fettiplace R, Hackney CM. The sensory and motor roles of auditory hair cells. Nat Rev Neurosci 2006, 7: 19–29.
2. Johnson SL, Eckrich T, Kuhn S, Zampini V, Franz C, Ranatunga KM, *et al.* Position-dependent patterning of spontaneous action potentials in immature cochlear inner hair cells. Nat Neurosci 2011, 14: 711–717.
3. Babola TA, Li S, Gribizis A, Lee BJ, Issa JB, Wang HC, *et al.* Homeostatic control of spontaneous activity in the developing auditory system. Neuron 2018, 99: 511–524 e515.
4. Tritsch NX, Rodriguez-Contreras A, Crins TT, Wang HC, Borst JG, Bergles DE. Calcium action potentials in hair cells pattern auditory neuron activity before hearing onset. Nat Neurosci 2010, 13: 1050–1052.
5. Marcotti W, Johnson SL, Kros CJ. A transiently expressed SK current sustains and modulates action potential activity in immature mouse inner hair cells. J Physiol 2004, 560: 691–708.
6. Johnson SL, Adelman JP, Marcotti W. Genetic deletion of SK2 channels in mouse inner hair cells prevents the developmental linearization in the $Ca^{2+}$ dependence of exocytosis. J Physiol 2007, 583: 631–646.
7. Evans MG, Fuchs PA. Tetrodotoxin-sensitive, voltage-dependent sodium currents in hair cells from the alligator cochlea. Biophys J 1987, 52: 649–652.
8. Marcotti W, Johnson SL, Rusch A, Kros CJ. Sodium and calcium currents shape action potentials in immature mouse inner hair cells. J Physiol 2003, 552: 743–761.
9. D OM, Hudspeth AJ. Effects of cochlear loading on the motility of active outer hair cells. Proc Natl Acad Sci USA 2013, 110: 5474–5479.
10. Oliver D, Plinkert P, Zenner HP, Ruppersberg JP. Sodium current expression during postnatal development of rat outer hair cells. Pflugers Arch 1997, 434: 772–778.
11. Housley GD, Marcotti W, Navaratnam D, Yamoah EN. Hair cells–beyond the transducer. J Membr Biol 2006, 209: 89–118.
12. Catterall WA. From ionic currents to molecular mechanisms: the structure and function of voltage-gated sodium channels. Neuron 2000, 26: 13–25.
13. Yu FH, Yarov-Yarovoy V, Gutman GA, Catterall WA. Overview of molecular relationships in the voltage-gated ion channel superfamily. Pharmacol Rev 2005, 57: 387–395.
14. Zhou Y, Ji Y. Voltage-gated sodium channels involve in sensory information processing. CNS Neurol Disord Drug Targets 2018.
15. Masetto S, Bosica M, Correia MJ, Ottersen OP, Zucca G, Perin P, *et al.* Na+ currents in vestibular type I and type II hair cells of the embryo and adult chicken. J Neurophysiol 2003, 90: 1266–1278.
16. Wooltorton JR, Gaboyard S, Hurley KM, Price SD, Garcia JL, Zhong M, *et al.* Developmental changes in two voltage-dependent sodium currents in utricular hair cells. J Neurophysiol 2007, 97: 1684–1704.
17. Eckrich T, Varakina K, Johnson SL, Franz C, Singer W, Kuhn S, *et al.* Development and function of the voltage-gated sodium current in immature mammalian cochlear inner hair cells. PLoS One 2012, 7: e45732.
18. Zhou Y, Fang FH, Liu ZR, Ji YH. Dissection of voltage-gated sodium channels in developing cochlear sensory epithelia. Protein Cell 2015, 6: 458–462.
19. Blaustein MP, Goldman DE. The action of certain polyvalent cations on the voltage-clamped lobster axon. J Gen Physiol 1968, 51: 279–291.
20. Blanton MG, Kriegstein AR. Spontaneous action potential activity and synaptic currents in the embryonic turtle cerebral cortex. J Neurosci 1991, 11: 3907–3923.
21. Soto F, Ma X, Cecil JL, Vo BQ, Culican SM, Kerschensteiner D. Spontaneous activity promotes synapse formation in a cell-type-dependent manner in the developing retina. J Neurosci 2012, 32: 5426–5439.
22. Mooney R, Penn AA, Gallego R, Shatz CJ. Thalamic relay of spontaneous retinal activity prior to vision. Neuron 1996, 17: 863–874.
23. Murase S, Owens DF, McKay RD. In the newborn hippocampus, neurotrophin-dependent survival requires spontaneous activity and integrin signaling. J Neurosci 2011, 31: 7791–7800.
24. Lippe WR. Rhythmic spontaneous activity in the developing avian auditory system. J Neurosci 1994, 14: 1486–1495.
25. Johnson SL, Kuhn S, Franz C, Ingham N, Furness DN, Knipper M, *et al.* Presynaptic maturation in auditory hair cells requires a critical period of sensory-independent spiking activity. Proc Natl Acad Sci USA 2013, 110: 8720–8725.
26. Marcotti W, Kros CJ. Developmental expression of the potassium current IK,n contributes to maturation of mouse outer hair cells. J Physiol 1999, 520: 653–660.
27. Marcotti W, Johnson SL, Kros CJ. Effects of intracellular stores and extracellular Ca(2+) on Ca(2+)-activated K(+) currents in mature mouse inner hair cells. J Physiol 2004, 557: 613–633.
28. Hackney CM, Mahendrasingam S, Penn A, Fettiplace R. The concentrations of calcium buffering proteins in mammalian cochlear hair cells. J Neurosci 2005, 25: 7867–7875.
29. Dou H, Vazquez AE, Namkung Y, Chu H, Cardell EL, Nie L, *et al.* Null mutation of alpha1D $Ca^{2+}$ channel gene results in deafness but no vestibular defect in mice. J Assoc Res Otolaryngol 2004, 5: 215–226.
30. Sangameswaran L, Fish LM, Koch BD, Rabert DK, Delgado SG, Ilnicka M, *et al.* A novel tetrodotoxin-sensitive, voltage-gated sodium channel expressed in rat and human dorsal root ganglia. J Biol Chem 1997, 272: 14805–14809.
31. Cummins TR, Howe JR, Waxman SG. Slow closed-state inactivation: a novel mechanism underlying ramp currents in cells expressing the hNE/PN1 sodium channel. J Neurosci 1998, 18: 9607–9619.
32. Waxman SG. Neurobiology: a channel sets the gain on pain. Nature 2006, 444: 831–832.
33. Blair NT, Bean BP. Roles of tetrodotoxin (TTX)-sensitive $Na^+$ current, TTX-resistant $Na^+$ current, and $Ca^{2+}$ current in the action potentials of nociceptive sensory neurons. J Neurosci 2002, 22: 10277–10290.
34. Patino GA, Isom LL. Electrophysiology and beyond: multiple roles of $Na^+$ channel beta subunits in development and disease. Neurosci Lett 2010, 486: 53–59.
35. Ophoff RA, Terwindt GM, Vergouwe MN, van Eijk R, Oefner PJ, Hoffman SM, *et al.* Familial hemiplegic migraine and episodic ataxia type-2 are caused by mutations in the $Ca^{2+}$ channel gene CACNL1A4. Cell 1996, 87: 543–552.
36. Plummer NW, McBurney MW, Meisler MH. Alternative splicing of the sodium channel SCN8A predicts a truncated two-domain protein in fetal brain and non-neuronal cells. J Biol Chem 1997, 272: 24008–24015.
37. Chatelier A, Dahllund L, Eriksson A, Krupp J, Chahine M. Biophysical properties of human Nav1.7 splice variants and their regulation by protein kinase A. J Neurophysiol 2008, 99: 2241–2250.